AIAA 2013-2919

A Study of Burst Wakes in a Multielement Airfoil Flowfield

Brent W. Pomeroy*, Phillip J. Ansell†, Jeffrey M. Diebold‡, and Michael S. Selig§
University of Illinois at Urbana-Champaign, Department of Aerospace Engineering, Urbana, IL 61801

High lift multielement airfoils, such as those used on large transport aircraft during takeoff and landing, can generate strong adverse pressure gradients that, while the surface flow is attached, can cause off-the-surface separation in the wake, so called, wake bursting. The sudden expansion and thickening of the separated wakes has been shown to decrease lift and increase drag. Wake bursting was experimentally studied over a three-element high lift airfoil, and unsteady velocity measurements were taken with a split film probe. The tests were performed in the University of Illinois low-speed low-turbulence subsonic wind tunnel on a multielement airfoil having a chord length of 1.35 ft (0.411 m) and a model span of 2.8 ft (0.85 m). Results for a Reynolds number of 1×10^6 indicate that wake bursting was observed for the wake of the main element and the first flap. A methodology was developed to numerically define the core of each wake both upstream and downstream of the burst point. Data show that the local flowfield angle in the wake core does not significantly change relative to the flowfield outside the wake core. Unsteady results indicate that the velocity fluctuations within the burst wake region are dominated by turbulence in the shear layers between the wakes with less turbulence observed in the wake cores. These turbulent fluctuations were largest in the shear layers and were observed to spread into the wake cores.

Nomenclature

c_n	=	chord length of element n
C_d	=	airfoil drag coefficient
C_l	=	airfoil lift coefficient
E	=	probe voltage
P	=	pressure
U_t	=	magnitude of total velocity $\sqrt{u^2+v^2}$
u	=	chordwise velocity component
u'	=	time-dependent fluctuation in u
v	=	chord-normal velocity component
v'	=	time-dependent fluctuation in v
α	=	angle of attack
δ	=	flap deflection angle
ρ	=	density
ϕ	=	time-averaged local flow angle
θ	=	local flow angle

Subscripts

cor	=	corrected value
cal	=	calibration data point
f	=	local freestream value
le	=	leading edge
n	=	parameter relating to element n
r	=	rotated coordinate system
ref	=	reference condition

*Graduate Research Fellow, Department of Aerospace Engineering, 104 S. Wright St., AIAA Student Member.
†Graduate Research Assistant, Department of Aerospace Engineering, 104 S. Wright St., AIAA Student Member.
‡Graduate Research Assistant, Department of Aerospace Engineering, 104 S. Wright St., AIAA Student Member.
§Associate Professor, Department of Aerospace Engineering, 104 S. Wright St., AIAA Senior Member.

t = total value
unc = uncorrected value
w = value in wake
∞ = freestream conditions

I. Introduction

The aerodynamics of multielement high lift devices is complex and can be greatly impacted by wakes in an adverse pressure gradient. In addition to the shape and location of each element, the wake of the main element, the jet through the gaps, and the flap wake can also have a large effect on the flowfield.[1,2] If a strong adverse pressure gradient is imposed on a multielement airfoil, a wake may experience off-the-surface separation, or "wake bursting," while the flow along the surface remains attached. Wake bursting is a local deceleration of the flow in the wake of one or more of the elements.

A conceptual sketch of a burst-wake region is presented in Fig. 1. As shown in the drawing, a wake from an element may rapidly thicken and decelerate because of the strong adverse pressure gradient. Both the main element wake and first flap wake are burst in the sketch. Burst wakes are characterized by rapid wake thickening, flow deceleration, and increased turbulence.[3–5] In general, performance decreases if the wakes of the main element and the flaps become confluent, i.e. if they merge. Research indicates that merging flows and "off-the-surface separation" can dominate the flowfield.[1,6,7]

Wake bursting, as first discussed by Smith,[1] is a viscous phenomenon, leading to increased drag (C_d), a reduction of maximum lift $(C_{l,max})$, an effective decambering of the airfoil system, and sometimes flow reversal in the wake.[4,5,8,9] As expected, the pressure distribution of a multielement airfoil can be driven by the wakes in addition to the shape and location of the flap elements.[3,6,10] In fact, if the wakes merge, it has been shown that the momentum deficit in the wakes can dominate the flowfield.[6,11–13] Research performed in the NASA Langley Low Turbulence Pressure Tunnel (LTPT) indicates that the development of a wake is highly dependent on the Reynolds number of the flow and that a lower Reynolds number can result in larger wakes and more off-the-surface flow reversal.[7] Also, wake bursting is dependent on Mach number.[14] Some previous tests investigated the burst wake of a flat plate with a single flap in an adverse pressure gradient imposed by moveable tunnel walls with no flow curvature.[9,15–17] These flat plate tests concluded that turbulence intensity and wake thickness both increased with a stronger adverse pressure gradient. Experimental investigations have not captured full-field measurements of wake bursting over a multielement airfoil at lower Reynolds numbers and efforts have not been made to clearly define the edge of a wake in a curved flowfield with an adverse pressure gradient. In addition, turbulence measurements have not been made for a continuous set of coordinates in a burst wake region over a multielement airfoil.

The objective of this study was to experimentally capture wake bursting over a multielement airfoil system using off-body measurement techniques. The goal was to identify an airfoil at a condition for which the flow was attached to the surface of all elements but where bursting was present. Additionally, this project has aimed to identify the location of the wake cores and the characteristics of the flow within the wake cores. Finally, turbulence levels in the shear layers of the flow were compared with the turbulence levels in the wake cores.

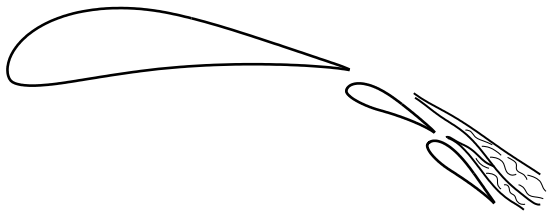

Figure 1. Conceptual sketch of wake bursting over a high lift multielement airfoil.

II. Airfoil Geometry and Coordinate Systems

A three-element airfoil system, the MFFS(ns)-026, was examined in this research. The MFFS(ns)-026 airfoil as shown in Fig. 2 is similar to the multielement system presented in Ref. 18 with the difference being that the flaps are in different positions. As seen in Fig. 2, the airfoil system is shown at $\alpha = 0$ deg with a system chord length of 1. It is defined that $\alpha = 0$ deg when the leading edge and trailing edge of the main element lie on the x axis as depicted. The system chord line is defined as the distance from the leading edge of the main element to the trailing edge of the last element projected along the main element chord line.

A coordinate system was used to define the location of each element in terms of leading edge coordinate $(x,y)_{le,n}$ and deflection angle δ_n (see Fig. 3). The deflection angle of each flap element is defined relative to the main element chord line, and a positive deflection angle corresponded to a downward flap deflection. The dimensional chord length of the main element (c_1) was 11.5 in (292 mm), the chord length of the first flap (c_2) was 3.5 in (88 mm), and the chord length of the second flap (c_3) was 3.0 in (76 mm). Nondimensional chord lengths were obtained by dividing the chord length of each element (c_n) by the system chord length which was taken as 16.36 in (415 mm). Table 1 shows the nondimensional chord lengths, nondimensional leading edge coordinates, and deflection angles of each element. The reference area was defined as the projected area of the multielement system. Airfoil coordinates for each element are presented in Appendix A.

In addition, a relative coordinate system, as shown in Fig. 4, could be used to define the system by parameters that govern the flow including gap size and overhang distance. The gap size between elements (gap_n) was defined as the distance from the trailing edge of element n to the closest point on element $n+1$. The overhang distance $(overhang_n)$ between element n and $n+1$ was defined as the distance from the leading edge of element $n+1$ to the trailing edge

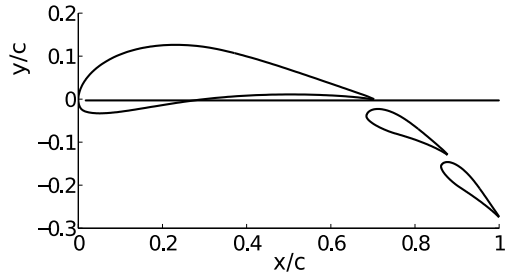

Figure 2. MFFS(ns)-026 three-element airfoil at $\alpha = 0$-deg.

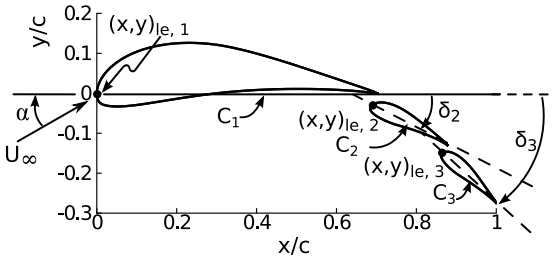

Figure 3. Absolute coordinate system used to define the three-element airfoil geometry investigated in this study.

Table 1. Location of Elements in Airfoil System in Absolute Coordinates

	Main Element	Flap 1	Flap 2
c/c_{sys}	0.7028	0.2139	0.1834
$(x,y)_{le}$	$(0,0)$	$(0.6860,-0.0344)$	$(0.8644,-0.1510)$
δ	–	26.43 deg	42.32 deg

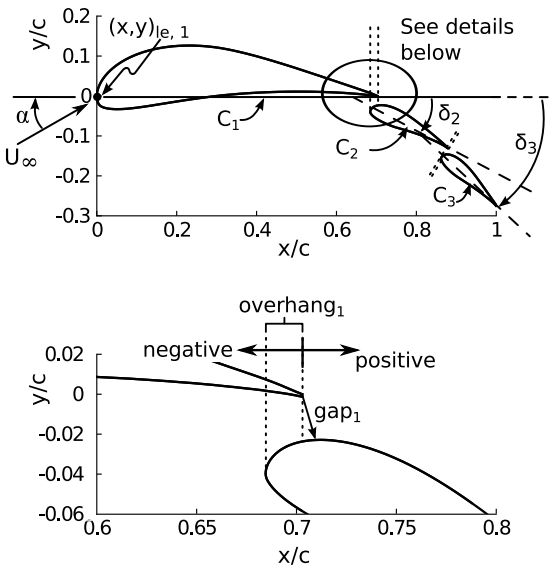

Figure 4. Relative coordinate system used to define the three-element airfoil geometry investigated in this study.

Table 2. Location of Elements in Airfoil System in Relative Coordinates

	Main Element to Flap 1	Flap 1 to Flap 2
gap/c_{sys}	0.0100	0.0100
$overhang/c_{sys}$	0.0150	0.0150

of n projected along the chord line of element n, as shown in the lower portion of Fig. 4. Nondimensional relative coordinate values for the MFF(S)-026 are presented in Table 2.

III. Experimental Methods

Aerodynamic tests were performed in the University of Illinois low-speed low-turbulence wind tunnel as sketched in Fig. 5. The tunnel is an open-return-type wind tunnel, and the rectangular cross section is 2.8 ft (0.85 m) by 4.0 ft (1.22 m) and 8.0 ft (2.44 m) long. The downstream location of the test section is 0.5 in (1.3 cm) wider than the upstream end to account for boundary layer growth along the walls. To ensure good flow quality, the air passes through a 4-in (10.2 cm) thick honeycomb mesh, four stainless steel anti-turbulence screens, and a 7.5:1 inlet contraction. The presence of these screens and flow conditioning reduces the empty test section turbulence intensity to less than 0.1% at all operating speeds.[19] The speed of the tunnel was set by a five-blade metal fan driven by a 125-HP AC motor that was controlled by an ABB ACS 800 Low Voltage AC Drive. A maximum fan speed of 1,200 RPM creates a test section flow speed of approximately 165 mph (74 m/sec) or a maximum Reynolds number of 1.45×10^6/ft (4.75×10^6/m), yielding a maximum Reynolds number of 1.98×10^6 for the current 16.36-in chord model. The speed was computer controlled to maintain a Reynolds number of 1.00×10^6 during all tests reported in this paper. An external, floor-mounted, three-component balance was used to measure lift, drag, and pitching moment of the airfoil system. Drag data were also taken using a wake rake traverse system. A set of 59 total pressure probes were installed in the wake rake, and pressure data were measured with a DTC Initium system and two ± 0.35 psi 32-port pressure modules. The wake profile was used to determine the drag as discussed by Jones and Schlichting.[20,21] Cylindrical-tip total pressure probes were used in this project and previous research indicates that simple total pressure probes accurately capture drag using the Jones method in highly turbulent wakes with separation[22]. Methods presented by Barlow, et al.[23] were used to correct the wind tunnel measurements for wind tunnel wall effects. Only airfoil profile drag is reported in this paper, and moment data are not reported.

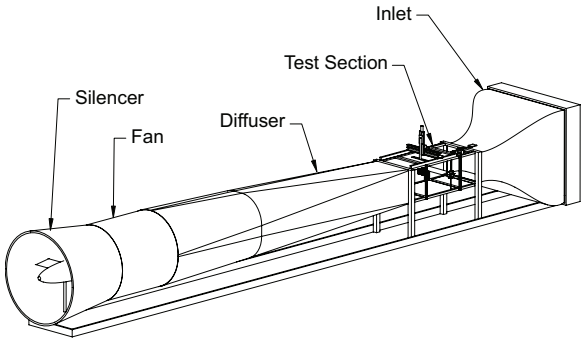

Figure 5. University of Illinois 2.8 × 4 ft low-speed low-turbulence subsonic wind tunnel.

Figure 6. Experimental setup of sidewall-mounted traverse with three-element airfoil model installed.

Fluorescent surface oil flow visualization was used to ascertain whether or not the flow was attached on the surface of all three elements. Flow visualization was performed by first applying a very thin layer of 5W-30 motor oil to the surface of the airfoil model. An airbrush was then used to apply a mixture of mineral oil and fluorescent leak detector dye to the surface of the model. Flowfield measurements were performed at a Reynolds number of 1.00×10^6 and $\alpha = 0.0$ deg. The locations of key flow features were measured by using a strip of yellow electrical tape that was marked with x/c coordinates in 5% increments. The wind tunnel was run at the desired Reynolds number for 4 minutes. Black lights were used to illuminate the fluorescent oil, and the results were documented with a digital camera for later post processing.

Measurements in the flowfield were taken using a split film probe attached to a two-axis Lintech traverse system mounted on the sidewall of the tunnel as shown in Fig. 6. Both arms of the traverse extended into the test section, and the split film was mounted on the end of the lower arm. A diagonal support (upper arm) was attached to the traverse for added structural integrity. An external symmetric airfoil fairing was used to streamline the traverse arms and reduce potential vibration from vortex shedding. The tunnel was sealed with airtight rubber sleeves around the traverse arms together with a combination of teflon and metal plates on the side of the tunnel. Measurements were taken in the flowfield above the multielement airfoil (on the suction side) at a spatial resolution of 0.1 in (2.54 mm) while maintaining an offset distance of 0.25 in (6.35 mm) from the surface of the airfoil.

A two-component TSI 1288 split film probe controlled by a TSI IFA 100 constant temperature anemometer was used to determine the time-dependent velocity parallel to freestream flow (u) and orthogonal to freestream flow (v). As air passed over the constant temperature split film, the heat transfer affected the two films at different rates depending on the local flow angularity. The anemometer subsequently adjusted the voltage E of each film independently to maintain a constant temperature of each film. The magnitude of the two probe voltages relative to a baseline voltage and the difference in the excitation voltages between the two films are then used to calculate time-dependent u and v velocity components. The split film measurements were sampled simultaneously using a National Instruments SCXI

scanning system. These unsteady data were acquired at a sample rate of 3 kHz for 10 sec. In addition, data were filtered at the Nyquist cutoff frequency of 1.5 kHz using a low-pass Bessel filter. The total velocity uncertainty was determined to be 0.81% (0.97 ft/sec) and dimensional uncertainty in flow angularity θ was calculated to be 1.01 deg.

Calibration of the split film was performed as a function of freestream velocity and local flow angle θ. Standard methods discussed by Bruun[24] were used to correct the voltage of the films for temperature changes, viz

$$E_{cor} = E\sqrt{\frac{T_{wire} - T_{ref}}{T_{wire} - T_{amb}}} \tag{1}$$

where E_{cor} is the corrected probe voltage as a function of three temperatures, namely ambient temperature at the start of the calibration (T_{ref}), ambient temperature during the calibration (T_{amb}), and temperature of each film (T_{wire}). A calibration routine was performed at $\theta = 0$ deg over a range of freestream flow speeds to yield a polynomial for which $U_t = f(E_{cor})$. As documented by Bruun[24] as well as Siddal and Davies,[25] the probe voltages of the two films E_1 and E_2 can be related to U_t by

$$\left(\frac{E_1 + E_2}{2}\right)^2 = K(U_t) \tag{2}$$

where the function $K(U_t)$ was selected to be a fifth-order polynomial fit of the data. Work by Spring[26] based upon the ideal gas law was used to introduce a correction for differences in density from the calibration measurement and the acquired data point where

$$U_{t,cor} = \frac{\rho_{cal}}{\rho_{test}} U_{t,unc} \tag{3}$$

A second calibration to determine flowfield angularity was performed at one velocity for a range of θ measured relative to the plane of the split between the films. As discussed by Bruun[24] and Seung-Ho,[27] a calibration curve that is independent of velocity, denoted as $Z(\theta)$, can be determined. The calibration curve $Z(\theta)$ is a function of the probe voltages at two reference angles $E(\theta_{ref,1})$ and $E(\theta_{ref,2})$ and the probe voltages during the test $E(\theta)$. A calibration was performed for a range of θ values, and the corresponding $Z(\theta)$ value for each value of θ was calculated via

$$Z(\theta) = \frac{E_1(\theta) - E_1(\theta_{ref,1})}{E_1(\theta_{ref,2}) - E_1(\theta_{ref,1})} + \frac{E_2(\theta_{ref,1}) - E_2(\theta)}{E_2(\theta_{ref,1}) - E_2(\theta_{ref,2})} \tag{4}$$

A fifth-order polynomial fit was applied to the aforementioned calibration data to determine $Z(\theta)$ across a range of θ. For a given measurement, the values of E_1 and E_2 were used to calculate $K(U_t)$ and $Z(\theta)$ as presented in Eqs. 2 and 4. These values of $K(U_t)$ and $Z(\theta)$ were applied to the respective calibration curves to compute U_t and θ from which the velocity components u and v were decomposed.

IV. Results

An investigation was performed to identify an airfoil geometry (flap placements, see Table 1), and a set of operating conditions, which were determined to be $\alpha = 0$ deg and $Re = 1.00 \times 10^6$, for which the flow was attached to all three elements but where wake bursting was present. For this condition, aerodynamic data were acquired for time-averaged and time-dependent quantities. Time-averaged data included the lift and drag data, wake profiles, and surface flow visualization. Unsteady results included the total velocity, flow angularity, and turbulence levels.

A. Time-Averaged Results

Surface oil flow visualization results on the upper surface of the three-element airfoil at $\alpha = 0.0$ deg and $Re = 1.00 \times 10^6$ are presented in Fig. 7 where flow is from left-to-right in the photograph. As seen, a laminar separation bubble is visible on the main element between $x/c \approx 0.25$ and 0.29. The trailing edge of the main element is seen as an oil accumulation line at $x/c \approx 0.67$. A laminar separation bubble is present on the first flap between $x/c \approx 0.71$ and 0.73, and an oil accumulation at $x/c \approx 0.86$ indicates the trailing edge of the first flap. A laminar separation bubble on the second flap is present between $x/c \approx 0.89$ and 0.91. Thus, overall, there is no trailing-edge stall or massive separation. Hence, the flow is "well-behaved" and, in the context of this research, said to be attached.

Lift and drag data shown in Fig. 8 were collected over an angle of attack range from -4 to 7 deg in 1 deg increments, and it was observed that the stall angle is greater than 7 deg. It is noted that the lift curve slope, $C_{l\alpha}$, was calculated to be 0.0811 /deg, which is less than the theoretical value of 0.110 /deg predicted by thin airfoil theory. It is

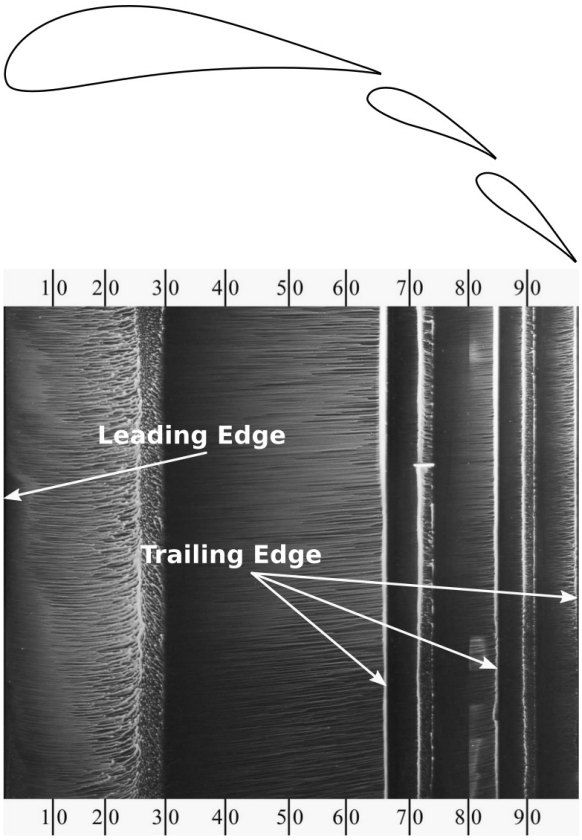

Figure 7. Surface oil flow visualization of MFFS(ns)-026 showing attached flow at $\alpha = 0$ deg and $Re = 1.0 \times 10^6$.

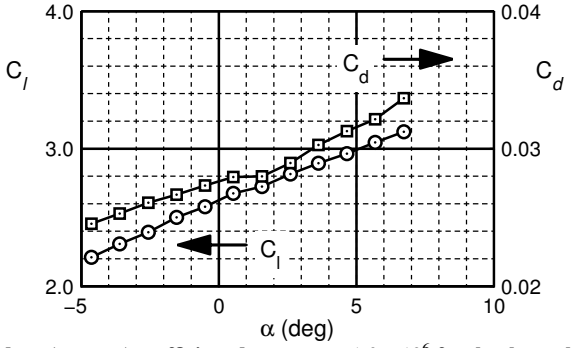

Figure 8. Lift (circles) and drag (squares) coefficient data at $Re = 1.0 \times 10^6$ for the three-element MFFS(ns)-026 airfoil.

possible that viscous effects in the burst wake region, to be discussed in later sections, reduce the value of $C_{l\alpha}$. Further research should be executed to determine the effect of burst wakes on airfoil performance. Both the flow visualization and the lift and drag data (Fig. 8) indicate that the flow is attached, and the system is not stalled between $\alpha = -4$ and 7 deg. Wake profiles were taken 1.88 chords (32.4 in, 0.823 m) downstream of the trailing edge of the model, and the wake profile at $\alpha = 0$ deg and $Re = 1.00 \times 10^6$ is shown in Fig. 9. The difference in total pressure $\Delta P_0 = P_{0,w} - P_{0,\infty}$ is plotted against chord-normal location in the wind tunnel (y). It is noted that the individual wakes from each element are not visible because the wakes merged and interacted to form one large wake at this downstream position.

B. Time-Averaged Velocity

Unsteady data were collected in the flowfield using the aforementioned split film probe and anemometer. Data were time-averaged for each point in the flowfield, and the resulting velocity measurements were normalized by U_∞. The

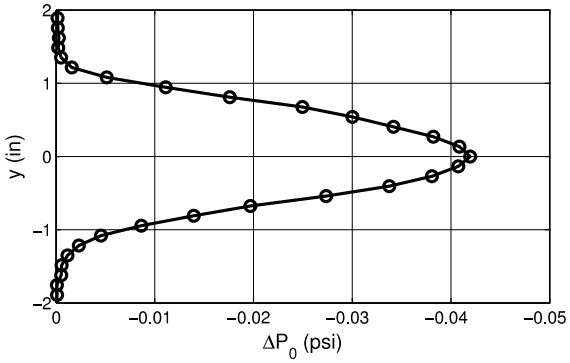

Figure 9. MFFS(ns)-026 wake profile 1.88 chords downstream of trailing edge at $\alpha = 0$ deg and $Re = 1.0 \times 10^6$.

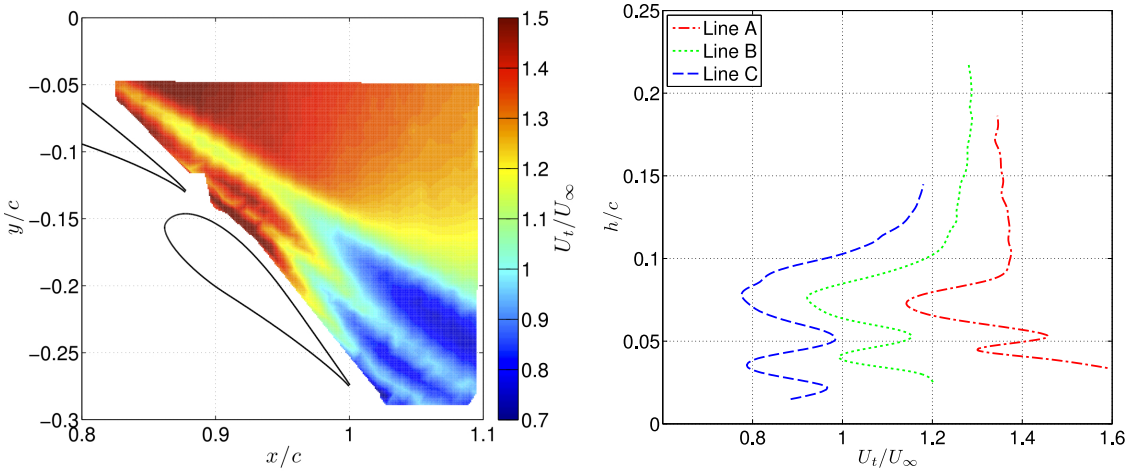

(a) (b)

Figure 10. Results of time-averaged U_t/U_∞ velocity in (a) contour plot and (b) selected line profiles.

resulting U_t/U_∞ values are contour plotted in Fig. 10 for $\alpha = 0$ deg and $Re = 1.00 \times 10^6$. All time-dependent results in this paper were acquired at this Reynolds number and angle of attack. The trailing portion of the first flap is visible, and the entirety of the second flap is shown; the main element is not shown. A contour plot is presented in Fig. 10(a), and three line plots are plotted in Fig. 10(b). Line profiles presented in Fig. 10(b) were taken normal to the chord line of flap 2 at three different locations, as shown in Fig. 11, and distance h was defined as the perpendicular distance from the flap 2 chord line.

The flowfield indicates wake bursting of both the main element wake and the wake of the first flap. The wake from the main element (visible in the upper left corner of the plot) bursts at $x/c \approx 0.96$ and $y/c \approx -0.13$. At this point, the wake begins to rapidly expand, and the velocity in the wake core also decreases to a minimum time-averaged velocity of $0.7U_\infty$. As compared with a non-burst wake, the main element burst wake is much wider and characterized by a greater velocity deficit. Similarly, the wake from the first flap originates near $x/c \approx 0.88$ and $y/c \approx -0.13$, and bursting occurs at $x/c \approx 0.95$ and $y/c \approx -0.17$. Both wakes burst at approximately the same x/c location. The wakes continue to spread further downstream from the burst locations and then they begin to interact at $x/c \approx 0.97$ and become one thick merged wake upstream of the wake rake (see Fig. 9). The growth of the wakes is not symmetrical about their respective centerlines, and the growth rate is diminished after the wakes first merge.

C. Wake Cores

Results presented in Fig. 10 indicate there is a distinct center region of each wake, and new criterion have been developed to extract the central portion of the wake (referred to as the "wake core"). Representative wake profiles

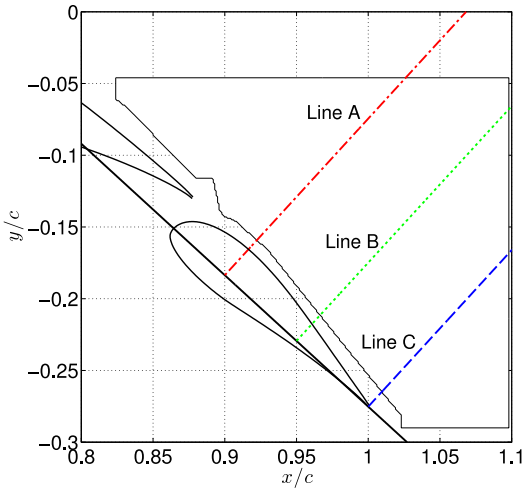

Figure 11. Position of extracted line-plot profiles.

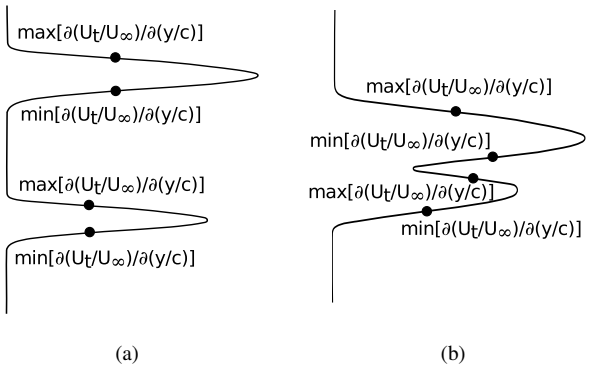

(a) (b)

Figure 12. Representative sketches and wake core edges for (a) non-confluent velocity profile and (b) confluent velocity profile.

extracted at a constant x/c location are shown in Fig. 12(a) for an x/c location upstream of where the wakes mix while wake profiles that have merged are shown in Fig. 12(b).

A methodology was developed to numerically extract the core of each wake based upon maximum and minimum values of the chord-normal velocity gradient ($\partial(U_t/U_\infty)/\partial(y/c)$) shown in Fig. 12. At a constant value of x/c, the chord-normal velocity gradient was calculated, and the local maximum value and minimum values defined the upper and lower edge of the wake core respectively. A contour map of $\partial(U_t/U_\infty)/\partial(y/c)$ is shown in Fig. 13(a), and the determined wake core edges are co-plotted as solid lines. Line-plots corresponding to $\partial(U_t/U_\infty)/\partial(y/c)$ are presented in Fig. 13(b). It is interesting to co-plot the wake core edges (defined in Fig. 12) with the time-averaged U_t/U_∞ velocity field shown in Fig. 14. The wake core edges follow the low momentum region in the flowfield. This observation suggests that the parameters chosen to define the wake core based upon $\partial(U_t/U_\infty)/\partial(y/c)$ also define the edge of the wake core adequately with respect to U_t/U_∞.

D. Time-Averaged Streamlines

The effect of wake bursting on the direction of the flow was studied, and the resulting streamlines based on u and v are co-plotted with U_t/U_∞ in Fig. 15. Distance between the streamlines in the wake core expand, indicating local flow deceleration, while spacing between the streamlines is smaller where the wake is not burst. It is observed that the streamlines do not follow the edge of a wake core, and this observation indicates that the burst wake region cannot be accurately predicted based upon the location of streamlines.

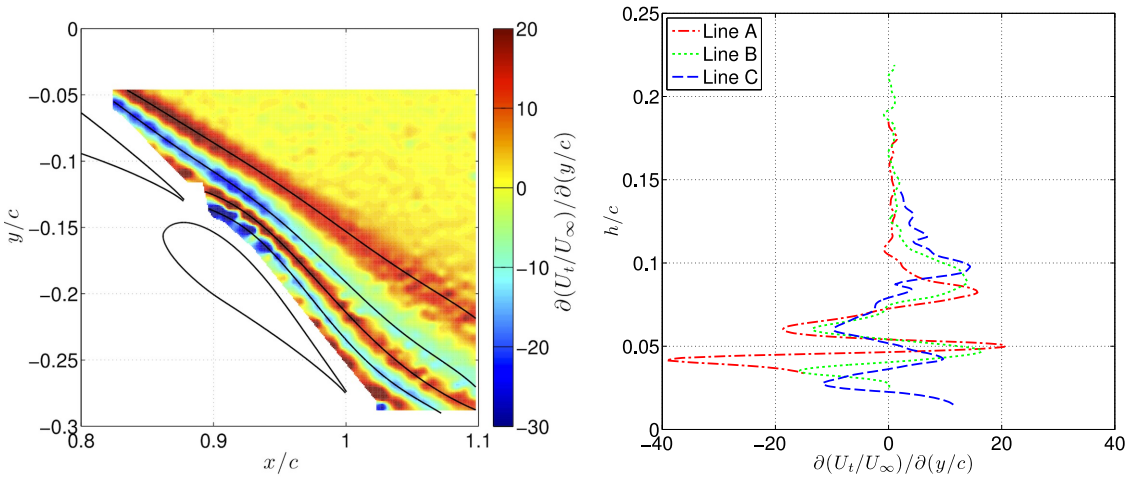

Figure 13. Chord-normal time-averaged velocity gradient $\partial(U_t/U_\infty)/\partial(y/c)$ in in (a) contour plot and (b) selected line profiles.

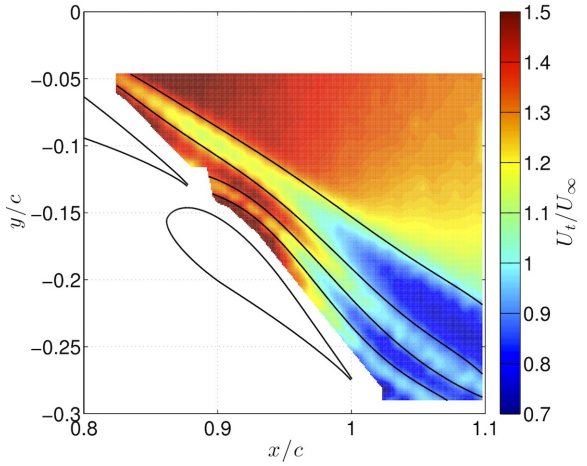

Figure 14. Contour plot of time-averaged U_t/U_∞ velocity with wake core edges.

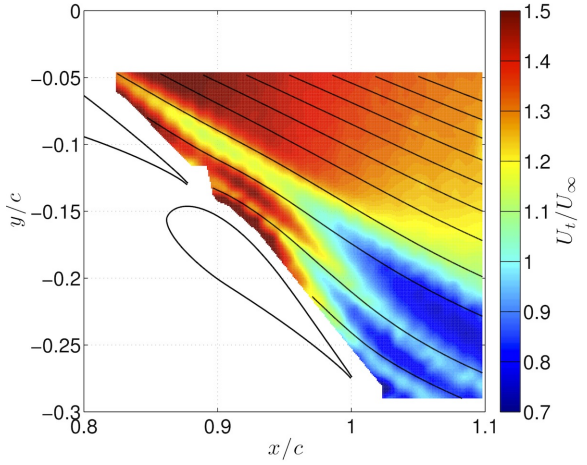

Figure 15. Streamlines and contour plot of time-averaged U_t/U_∞ velocity measurements.

E. Turbulence Parameters

Time-dependent measurements were taken, and the velocity fluctuations in the chordwise direction u' and chord-normal direction v' were used to determine turbulence intensities. Turbulence in the wake was characterized by the turbulent kinetic energy $(\overline{u'^2} + \overline{v'^2})/(2U_\infty^2)$, Reynolds stress $-\overline{u'v'}/U_\infty^2$, and a turbulent kinetic energy production term $\wp$ where

$$\wp = -2\frac{\overline{u'^2}}{U_\infty^2}\frac{\partial(u/U_\infty)}{\partial(x/c)} - 2\frac{\overline{v'^2}}{U_\infty^2}\frac{\partial(v/U_\infty)}{\partial(y/c)} - \frac{\overline{u'v'}}{U_\infty^2}\left(\frac{\partial(u/U_\infty)}{\partial(y/c)} + \frac{\partial(v/U_\infty)}{\partial(x/c)}\right) \tag{5}$$

Results for the turbulent kinetic energy (TKE) are presented in Fig. 16 while Reynolds stress and turbulent kinetic energy production are presented in Fig. 17. It is noted that the Reynolds shear stresses presented in Fig. 17(a) were calculated in a coordinate system which is aligned with the time-averaged local flow such that u_r was in the time-averaged direction of local flow and v_r was defined orthogonal to the direction of local flow. A rotation angle ϕ was defined to be equal to the time-averaged local flow angle $(\overline{\theta})$ at each spatial location where ϕ was defined to be positive when in the clockwise direction. Application of a simple rotation matrix yielded the Reynolds shear stress in the rotated reference frame to be

$$\frac{\overline{u_r'v_r'}}{U_\infty^2} = \frac{\overline{(u'\cos\phi - v'\sin\phi)(u'\sin\phi + v'\cos\phi)}}{U_\infty^2} \tag{6}$$

The turbulent kinetic energy is rotationally invariant and is unaffected by the coordinate system.

Wake core edges are co-plotted with turbulent kinetic energy (TKE) in Fig. 16. TKE levels are higher in the upper shear layer for both the main element and flap 1. Turbulence levels in the flap 1 wake, before the burst point, are greater than those in the main element wake before the main element wake bursts. Turbulence spreads into the main element wake core downstream of the burst point, and turbulence levels increase to as much as four times greater in the burst wake core than those in the non-burst core. TKE intensity increases more in the main element wake core than in the flap 1 wake core, and less TKE diffusion is observed in the flap 1 wake. High values of TKE do not follow the wake core edges, and the points of highest turbulence spread away from the upper edge of both wake cores at $x/c \geq 1.05$. Streamlines presented in Fig. 15 in the burst wake region indicate that the mean flow is convecting the turbulence away from the edge of the upper wake core edges.

In an effort to determine the origin of the turbulence in the flow, the Reynolds stress $-\overline{u'v'}/U_\infty^2$ and the turbulent kinetic energy production term $\wp$ were studied, as shown in Fig. 17. Regions of high turbulence production, $\wp$, are observed in the shear layers between the main element wake and the freestream as well as the shear layer between the wake of the main element and flap 1. This increase in turbulence production is a result of increased values of u' and v' as well as elevated values of normal and tangential velocity derivatives. The highest levels of turbulence production are observed to be in the shear layer between the wake cores of flap 1 and flap 2. Minimal or no turbulence production is observed in the wake cores. In addition, regions of high turbulence appear as discrete regions in the shear layer

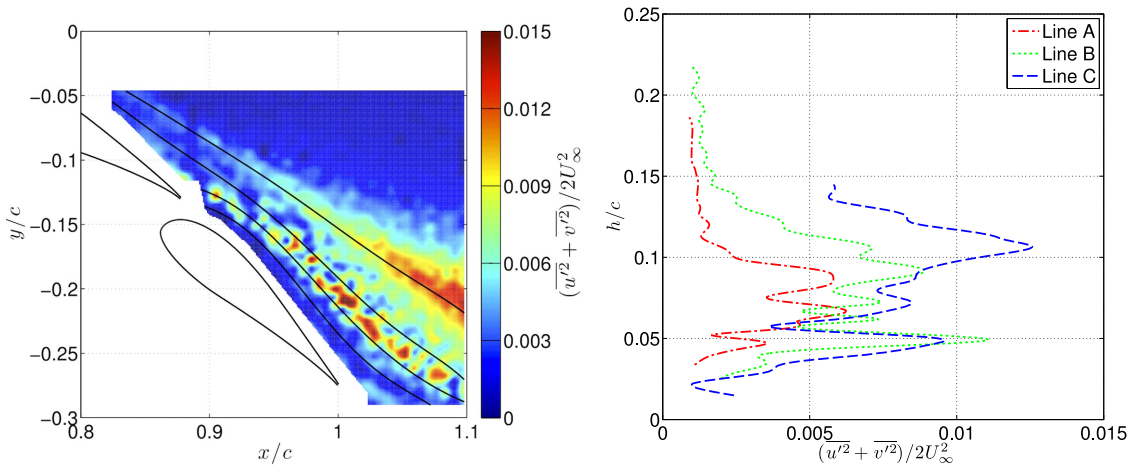

Figure 16. Turbulent kinetic energy $(\overline{u'^2} + \overline{v'^2})/2U_\infty^2$ in the flow with wake core edges.

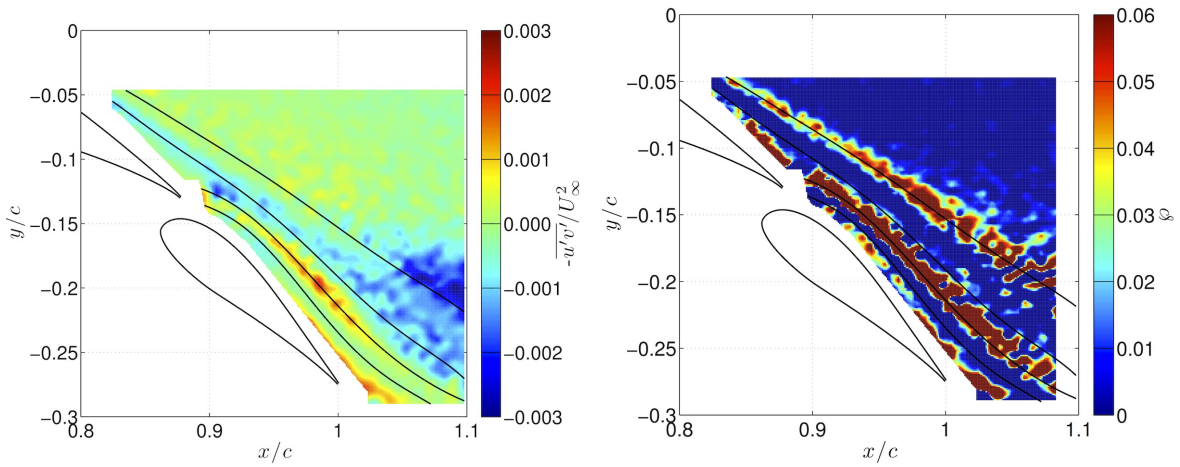

(a) (b)

Figure 17. Turbulence in flow with wake core edges as defined by (a) Reynolds stress $\overline{u'v'}$ and (b) turbulent kinetic energy production $\wp$.

between the core of the main element wake and the wake of flap 1. The discrete regions are observed in the TKE and Reynolds stress parameters. The regions are three to five times larger than the experimental spacing, so it is not believed that these regions are a consequence of the sampling grid. It is not known why these pockets exist as it is thought that the discrete region would disappear in the time-averaged turbulence.

F. Power Spectral Density

The unsteady behavior of the wake region was further investigated by analyzing the power spectral density (PSD) function of U_t/U_∞. Spectral content was analyzed along the wake core edge defined by the aforementioned methodology and in the chord-normal direction. The locations where PSDs were studied are shown in Fig. 18. The locations along the wake core edge are depicted by circles while the locations where the PSDs were studied across the wake, and wake core are depicted as squares. The Reynolds stresses and turbulent kinetic energy both suggest that most of the energy exists in the wake shear layers. Consequently, a comparison was made for the spectral content of U_t/U_∞ at different streamwise locations within the main element upper wake core edge, and results are presented in Fig. 19. The spectral content of U_t/U_∞ is primarily dominated by a frequency band of high energy density from 1 to 50 Hz at all six locations. The narrow frequency band corresponding to high energy density remains nearly constant with streamwise direction in the shear layer. However, the energy density within this frequency band increases with streamwise distance along the wake shear layer. By comparing Fig. 19(a) and (f) across the frequency band from 1 to 50 Hz, an increase in spectral density from -51 to -37 dB/Hz can be observed.

The spectral content of U_t/U_∞ was also compared at different chord-normal locations at a constant streamwise location of $x/c = 1.05$. Locations of interest are depicted by squares in Fig. 18, and the associated PSDs are presented in Fig. 20. Increased energy density from 1 to 50 Hz is only observed in Fig. 20(b) and (e) corresponding to points that were located in two different shear layers. It is observed that the energy density from 1 to 50 Hz decreases with increased distance from the main element shear layer, as evidenced in Fig. 20(a), (c–d), and (f). Spectral density in the shear layers of the main element was different than the energy in the shear layer of flap 1. The energy from 1 to 50 Hz in the shear layers of the main element, shown in Fig. 20(b,e), is larger than the energy in the flow from 1 to 50 Hz in the shear layer of flap 1 in Fig. 20(f).

The energy within the burst wake region was further characterized by integrating the PSD of U_t/U_∞ across the frequency band from 1 to 50 Hz. The resulting distribution of energy within the burst wake region across this frequency band is shown in Fig. 21. The results suggest that the regions corresponding to the greatest concentrations of energy are the wake shear layers from the main element. As previously mentioned, high turbulence intensities were also observed in these regions. Consequently, it is suggested that the turbulent characteristics of the wake shear layer are the primary contributors to the spectral content within the burst wake region.

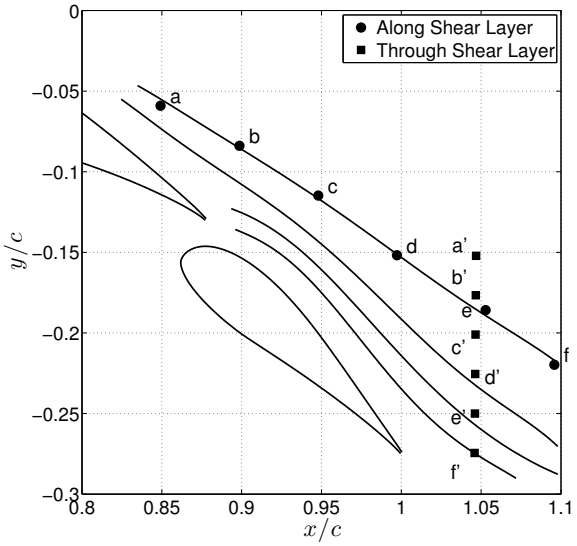

Figure 18. Location of points with selected power spectral densities.

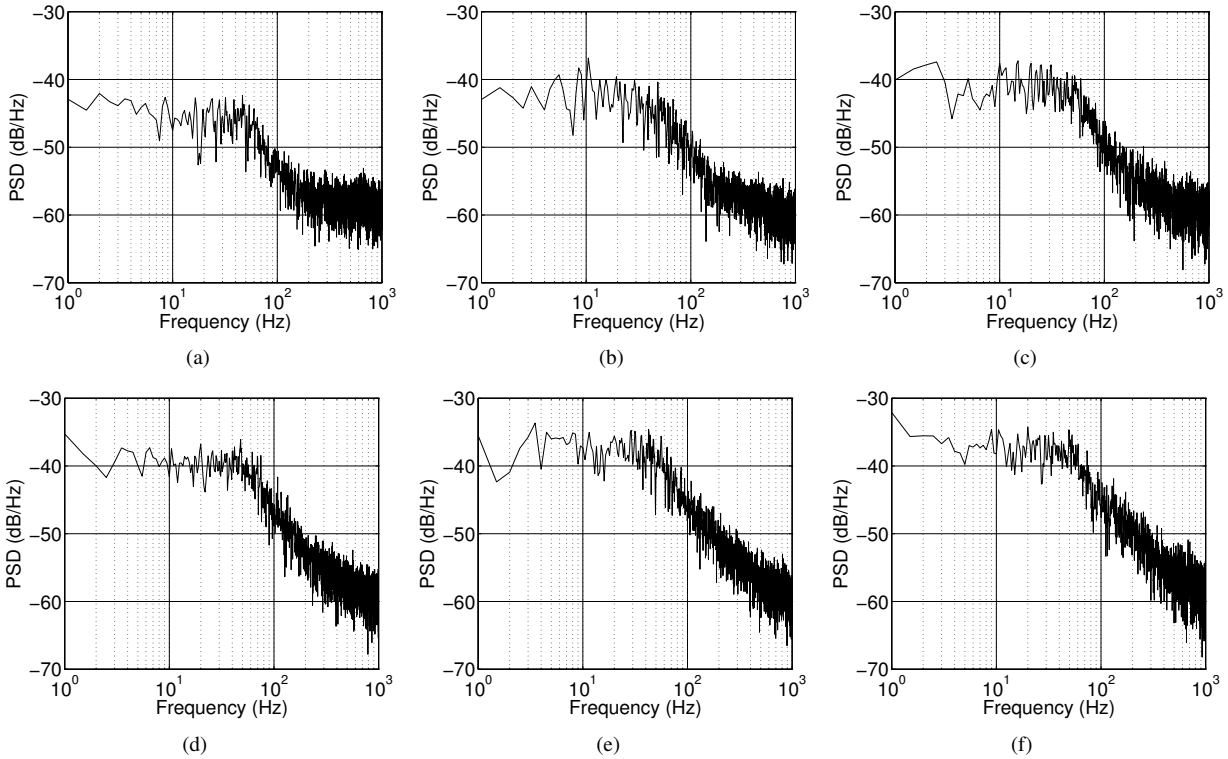

Figure 19. Power spectral density plots along main element upper wake core at (a) *x/c* = 0.85, (b) *x/c* = 0.90, (c) *x/c* = 0.95, (d) *x/c* = 1.00, (e) *x/c* = 1.05, and (f) *x/c* = 1.10.

V. Conclusions

Wind tunnel tests were carried out on the three-element MFFS(ns)-026 airfoil that exhibited wake bursting. Flow visualization was performed to ensure that the flow was attached to the surface of all three elements. An approach was developed and implemented to extract the edges of the wake cores of a multielement airfoil. Split film measurements were performed to measure time-dependent velocity in the flowfield of the burst wake region. Time-averaged results indicate that each wake core contains a large momentum-deficit region. Two clear cores were captured, and the wake development was analyzed upstream of the bursting point and downstream of the bursting point. The local flowfield angle in the wake core did not significantly change relative to that of the shear layer or in the freestream, but the

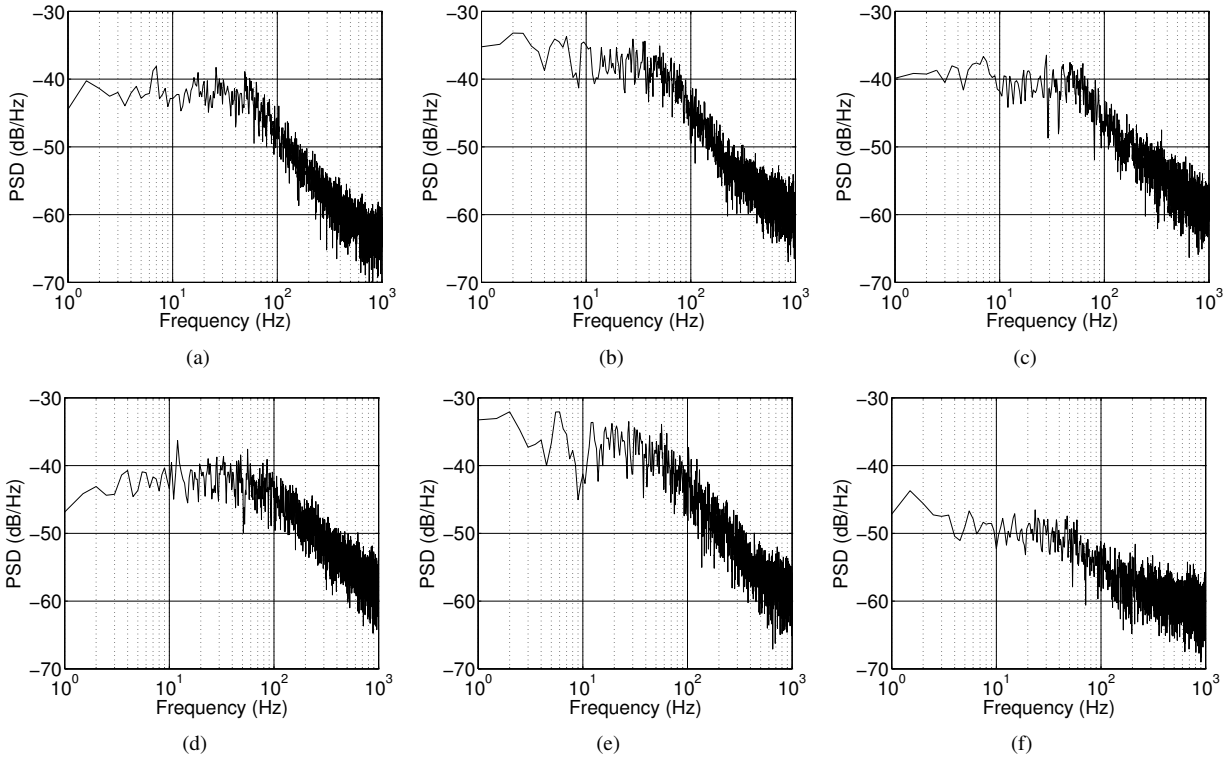

Figure 20. Power spectral density plots through shear layer at $x/c = 1.05$ and (a) $y/c = -0.15$, (b) $y/c = -0.175$, (c) $y/c = -0.20$, (d) $y/c = -0.225$, (e) $y/c = -0.25$, and (f) $y/c = -0.275$.

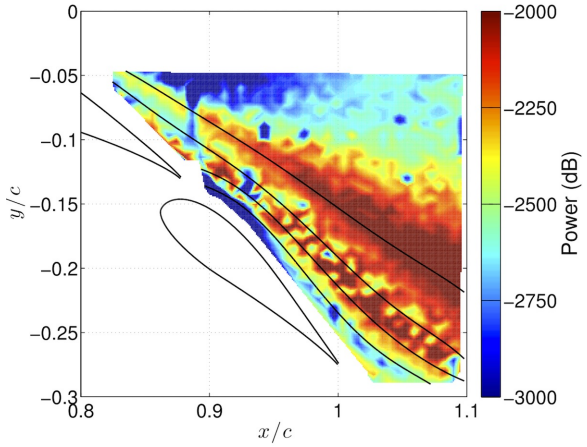

Figure 21. Integrated PSD energy from 1 to 50 Hz with wake core edges.

magnitude of the velocity vector was significantly reduced in the wake cores. Turbulence characteristics indicate that the majority of turbulence was produced in the region between the main element wake and the wake of flap 1. Analysis of the unsteady velocity power spectral density within the shear layers showed high energy density from 1 to 50 Hz that was not present outside the shear layers.

Acknowledgments

Support for this research project was provided by National Science Foundation graduate research fellowship grant number 07-15088 and the UIUC Department of Aerospace Engineering. Special thanks are also extended to Sean Cassidy for fabricating and maintaining the wind tunnel model as well as Dr. Michael Bragg for offering his invaluable guidance.

References

[1]Smith, A. M. O., "High-Lift Aerodynamics," *Journal of Aircraft*, Vol. 12, No. 6, 1975, pp. 501–530.

[2]van Dam, C. P., "The Aerodynamic Design of Multi-Element High-Lift Systems for Transport Airplanes," *Progress in Aerospace Sciences*, Vol. 38, 2002, pp. 101–144.

[3]Nakayama, A., Kreplin, H., and Morgan, H., "Experimental Investigation of Flowfield About a Multielement Airfoil," *AIAA Journal*, Vol. 28, No. 1, 1988, pp. 14–21.

[4]Driver, D. M. and Mateer, G. G., "Wake Flow in Adverse Pressure Gradient," *International Journal of Heat and Fluid Flow*, Vol. 23, 2002, pp. 564–571.

[5]Hoffenberg, R. and Sullivan, J. P., "Measurement and Simulation of Wake Deceleration," AIAA Paper 98-0522, AIAA Aerospace Sciences Meeting, Reno, NV, 1998.

[6]Rogers, S. E., "Progress in High-Lift Aerodynamic Calculations," *Journal of Aircraft*, Vol. 31, No. 6, 1994, pp. 1244–1251.

[7]Chin, V. D., "Flowfield Measurements about a Multi-Element Airfoil at High Reynolds Numbers," AIAA Paper 93-3137, AIAA Fluid Dynamics Conference, Orlando, FL, 1993.

[8]Klausmeyer, S. M. and Lin, J. C., "An Experimental Investigation of Skin Friction on a Multi-Element Airfoil," AIAA Paper 94-1870, AIAA Applied Aerodynamics Conference, Colorado Springs, CO, 1994.

[9]Hoffenberg, R. and Sullivan, J. P., "Simulation of High-Lift Wake Behavior," AIAA Paper 97-0718, AIAA Aerospace Sciences Meeting, Reno, NV, 1997.

[10]Spaid, F. W., "High Reynolds Number, Multielement Airfoil Flowfield Measurements," *Journal of Aircraft*, Vol. 37, No. 3, 2000, pp. 499–507.

[11]Cebeci, T., Besnard, E., and Chen, H. H., "Calculation of Multielement Airfoil Flows, Including Flap Wells," AIAA Paper 96-0056, AIAA Aerospace Sciences Meeting, Reno, NV, 1996.

[12]Czerwiec, R. and Edwards, J. R., "Theory and Experiment of Multielement Airfoils – A Comparison," AIAA Paper 2000-0985, AIAA Aerospace Sciences Meeting, Reno, NV, 2000.

[13]Narsipur, S., Pomeroy, B. W., and Selig, M. S., "CFD Analysis of Multielement Airfoils for Wind Turbines," AIAA Paper 2012-2781, AIAA Applied Aerodynamics Conference, New Orleans LA, 2012.

[14]Valarezo, W. O., Dominik, C. J., and McGhee, R. J., "Multielement Airfoil Performance Due to Reynolds and Mach Number Variations," *Journal of Aircraft*, Vol. 30, No. 5, 1993, pp. 689–694.

[15]Schneider, S., Campbell, B., Bucci, G., and Sullivan, J. P., "An Experimental Simulation of Flap Flow on Multielement Airfoils at High Reynolds Number," AIAA Paper 94-2613, AIAA Aerospace Ground Testing Conference, Colorado Springs, CO, 1994.

[16]Hoffenberg, R., Sullivan, J. P., and Schneider, S., "Wake Measurements in a Strong Adverse Pressure Gradient," NASA TR 197272, 1995.

[17]Bucci, G. S. and Sullivan, J. P., "An Experimental Simulation of High Lift Wake Flows at High Reynolds Number," AIAA Paper 97-2297, AIAA Applied Aerodynamics Conference, Atlanta, GA, 1997.

[18]Ragheb, A. M. and Selig, M. S., "Multi-Element Airfoil Configurations for Wind Turbines," AIAA Paper 2011-3971, AIAA Applied Aerodynamics Conference, Honolulu, HI, 2011.

[19]Selig, M. S. and McGranahan, B. D., "Wind Tunnel Aerodynamic Tests of Six Airfoils for Use on Small Wind Turbines," National Renewable Energy Laboratory, Golden, CO, NREL/SR-500-35515, 2004.

[20]Jones, B. M., "Measurement of Profile Drag by the Pitot-Traverse Method," British Aeronautical Research Council R&M 1688, London, England, 1936.

[21]Schlichting, H., *Boundary-Layer Theory*, McGraw-Hill Book Company, New York, 8th ed., 2000.

[22]Lu, B. and Bragg, M. B., "Experimental Investigation of the Wake-Survey Method for a Bluff Body with a Highly Turbulent Wake," AIAA Paper 2002-3060, Applied Aerodynamics Conference, St. Louis, MO, 2002.

[23]Barlow, J. B., Rae, Jr., W. H., and Pope, A., *Low-Speed Wind Tunnel Testing*, Wiley-Interscience, 3rd ed., 1999.

[24]Bruun, H. H., *Hot-Wire Anemometry*, Oxford Science Publications, New York, New York, 1995.

[25]Siddal, R. G. and Davies, T. W., "An Improved Response Equation for Hot-Wire Anemometry," *International Journal of Heat and Mass Transfer*, Vol. 15, No. 2, 1972, pp. 367–368.

[26]Spring, S. A., *An Experimental Mapping of the Flow Field Behind a Glaze Ice Shape on a NACA 0012 Airfoil*, Master's Thesis, Department of Mechanical and Aerospace Engineering, The Ohio State University, Columbus, OH, 1987.

[27]Seung-Ho, R., Chang, P. K., and Park, S. O., "A Modified Calibration Technique for the Split Film Sensor," *Journal of Measurement Science and Technology*, Vol. 1, No. 11, 1990, pp. 1076–1084.

Appendix A:
Multielement Airfoil Coordinates

In this appendix, coordinates for the MFF(S)-026 main element, flap 1, and flap 2 are given in Tables A.1, A.2, and A.3 respectively. All coordinates are normalized to a unit chord, but in assembly, the relative chord lengths and flap deflections were presented previously in Table 1.

Table A.1. MFF(ns)-026 Main Element Coordinates

1.0000	0.0009
0.9979	0.0017
0.9920	0.0042
0.9830	0.0080
0.9709	0.0125
0.9554	0.0179
0.9369	0.0243
0.9155	0.0315
0.8914	0.0396
0.8649	0.0485
0.8364	0.0581
0.8060	0.0683
0.7740	0.0790
0.7407	0.0899
0.7065	0.1011
0.6715	0.1122
0.6360	0.1231
0.6002	0.1336
0.5645	0.1436
0.5290	0.1528
0.4940	0.1611
0.4597	0.1682
0.4261	0.1737
0.3932	0.1775
0.3608	0.1798
0.3291	0.1805
0.2982	0.1798
0.2683	0.1776
0.2394	0.1741
0.2118	0.1691
0.1856	0.1629
0.1607	0.1555
0.1374	0.1469
0.1157	0.1373
0.0957	0.1267
0.0775	0.1153
0.0611	0.1031
0.0465	0.0904
0.0339	0.0771
0.0233	0.0637

Table A.1. MFF(ns)-026 Main Element Coordinates (continued)

0.0147	0.0500
0.0080	0.0364
0.0034	0.0231
0.0007	0.0102
0.0000	-0.0020
0.0013	-0.0133
0.0045	-0.0234
0.0096	-0.0314
0.0177	-0.0373
0.0293	-0.0415
0.0440	-0.0444
0.0617	-0.0458
0.0823	-0.0459
0.1059	-0.0446
0.1324	-0.0419
0.1619	-0.0381
0.1945	-0.0332
0.2299	-0.0275
0.2680	-0.0214
0.3086	-0.0150
0.3513	-0.0088
0.3958	-0.0028
0.4417	0.0026
0.4884	0.0070
0.5354	0.0106
0.5820	0.0132
0.6278	0.0150
0.6725	0.0161
0.7155	0.0164
0.7566	0.0162
0.7954	0.0154
0.8316	0.0142
0.8649	0.0126
0.8951	0.0108
0.9219	0.0088
0.9451	0.0067
0.9644	0.0046
0.9798	0.0026
0.9909	0.0009
0.9977	-0.0004
1.0000	-0.0009

Table A.2. MFF(ns)-026 Flap 1 Coordinates

1.0000	0.0029
0.9979	0.0035
0.9920	0.0055
0.9829	0.0088
0.9710	0.0130
0.9560	0.0177
0.9381	0.0230
0.9172	0.0287
0.8936	0.0350
0.8675	0.0418
0.8392	0.0490
0.8087	0.0566
0.7765	0.0644
0.7427	0.0725
0.7075	0.0806
0.6713	0.0888
0.6344	0.0969
0.5970	0.1048
0.5593	0.1123
0.5217	0.1195
0.4844	0.1260
0.4477	0.1317
0.4117	0.1364
0.3766	0.1401
0.3424	0.1426
0.3092	0.1438
0.2773	0.1438
0.2467	0.1425
0.2175	0.1399
0.1898	0.1361
0.1637	0.1310
0.1393	0.1248
0.1166	0.1175
0.0958	0.1091
0.0769	0.0999
0.0600	0.0898
0.0451	0.0791
0.0323	0.0678
0.0217	0.0560
0.0132	0.0439

Table A.2. MFF(ns)-026 Flap 1 Coordinates (continued)

0.0069	0.0315
0.0026	0.0191
0.0004	0.0070
0.0002	-0.0047
0.0021	-0.0156
0.0060	-0.0254
0.0128	-0.0334
0.0230	-0.0403
0.0361	-0.0466
0.0520	-0.0521
0.0704	-0.0568
0.0913	-0.0607
0.1146	-0.0636
0.1402	-0.0656
0.1679	-0.0666
0.1976	-0.0666
0.2292	-0.0657
0.2623	-0.0637
0.2969	-0.0607
0.3327	-0.0565
0.3700	-0.0506
0.4094	-0.0434
0.4508	-0.0360
0.4936	-0.0286
0.5372	-0.0217
0.5812	-0.0153
0.6251	-0.0097
0.6684	-0.0049
0.7106	-0.0009
0.7513	0.0023
0.7901	0.0046
0.8267	0.0061
0.8607	0.0068
0.8917	0.0069
0.9194	0.0063
0.9435	0.0051
0.9637	0.0034
0.9798	0.0014
0.9912	-0.0007
0.9979	-0.0023
1.0000	-0.0029

Table A.3. MFF(ns)-026 Flap 2 Coordinates

1.0000	0.0033
0.9979	0.0037
0.9917	0.0050
0.9819	0.0074
0.9689	0.0106
0.9527	0.0143
0.9334	0.0186
0.9110	0.0236
0.8858	0.0292
0.8582	0.0354
0.8282	0.0421
0.7963	0.0493
0.7626	0.0569
0.7275	0.0648
0.6912	0.0729
0.6541	0.0811
0.6164	0.0892
0.5784	0.0971
0.5404	0.1047
0.5028	0.1118
0.4656	0.1180
0.4290	0.1233
0.3931	0.1277
0.3580	0.1309
0.3240	0.1330
0.2911	0.1339
0.2595	0.1336
0.2293	0.1321
0.2005	0.1294
0.1734	0.1255
0.1480	0.1204
0.1244	0.1143
0.1027	0.1071
0.0829	0.0989
0.0652	0.0899
0.0496	0.0801
0.0362	0.0695
0.0249	0.0583
0.0158	0.0466
0.0087	0.0346
0.0037	0.0224
0.0008	0.0104
0.0000	-0.0013
0.0013	-0.0124
0.0046	-0.0224
0.0110	-0.0310
0.0206	-0.0388
0.0330	-0.0460
0.0481	-0.0526
0.0657	-0.0585
0.0857	-0.0636
0.1080	-0.0678
0.1325	-0.0711
0.1591	-0.0734
0.1876	-0.0747
0.2180	-0.0751
0.2499	-0.0743
0.2833	-0.0725
0.3179	-0.0694
0.3541	-0.0646
0.3923	-0.0585
0.4323	-0.0520
0.4737	-0.0453
0.5160	-0.0388
0.5587	-0.0326
0.6015	-0.0268
0.6438	-0.0215
0.6854	-0.0168
0.7257	-0.0127
0.7645	-0.0091
0.8014	-0.0062
0.8361	-0.0039
0.8682	-0.0022
0.8974	-0.0011
0.9235	-0.0005
0.9462	-0.0004
0.9652	-0.0007
0.9803	-0.0014
0.9913	-0.0022
0.9978	-0.0030
1.0000	-0.0033

Table A.3. MFF(ns)-026 Flap 2 Coordinates (continued)